J. Fluid Mech. (2025), *vol.* 1008, R1, doi:10.1017/jfm.2025.135

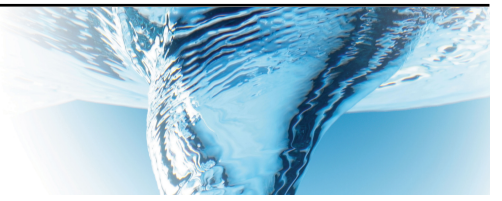

Taylor rolls on tour: slow drift of turbulent large-scale structures in flows with continuous symmetries

Daniel Feldmann[1] **and Marc Avila**[1,2]

[1]Center of Applied Space Technology and Microgravity (ZARM), University of Bremen, Am Fallturm 2, 28359 Bremen, Germany

[2]MAPEX Center for Materials and Processes, University of Bremen, Am Biologischen Garten 2, 28359 Bremen, Germany

Corresponding authors: Daniel Feldmann, daniel.feldmann@zarm.uni-bremen.de; Marc Avila, marc.avila@zarm.uni-bremen.de

(Received 9 December 2024; revised 24 January 2025; accepted 25 January 2025)

In Rayleigh–Bénard convection and Taylor–Couette flow cellular patterns emerge at the onset of instability and persist as large-scale coherent structures in the turbulent regime. Their long-term dynamics has been thoroughly characterised and modelled for the case of turbulent convection, whereas turbulent Taylor rolls have received much less attention. Here we present direct numerical simulations of axisymmetric Taylor–Couette flow in the corotating regime and reveal a transition to spatio–temporal chaos as the system size increases. Beyond this transition, Taylor rolls suddenly undergo erratic drifts evolving on a very slow time scale. We estimate an effective diffusion coefficient for the drift and compare the dynamics with analogous motions in Rayleigh–Bénard convection and Poiseuille flow, suggesting that this spontaneous diffusive displacement of large coherent structures is common among different types of wall-bounded turbulent flows.

Key words: Taylor–Couette flow, Bénard convection, plumes/thermals, rotating flows

1. Introduction

The smallest eddies in turbulent flows are dictated by the fluid's kinematic viscosity (ν) and dissipation, whereas the largest ones are shaped by the flow geometry, boundary conditions and source of driving. Very large coherent motions in the flow field (superstructures) carry a substantial part of the kinetic energy, which increases as

the Reynolds number (*Re*) increases (Smits *et al.* 2011). Understanding their role in transport and mixing is an active field of research, with many open questions relevant for predicting and modelling environmental fluid flows (Dauxois *et al.* 2021). In systems with linear instabilities, such as Rayleigh–Bénard convection (RBC) and Taylor–Couette flow (TCF), the origin of turbulent superstructures can be traced down to the onset of hydrodynamic instability. For TCF, Taylor rolls emerge from the primary instability of circular Couette flow (Taylor 1923), and then undergo a sequence of bifurcations (Coles 1965; Fenstermacher *et al.* 1979; Prigent *et al.* 2006), which increases the spatio–temporal complexity of the flow as *Re* increases (Feldmann *et al.* 2023). Seemingly, they persist in the form of turbulent Taylor rolls up to the highest *Re* investigated to date (Lathrop *et al.* 1992; Ravelet *et al.* 2010; Huisman *et al.* 2014; Ostilla-Mónico *et al.* 2016*a*; Sacco *et al.* 2019). We refer to Grossmann *et al.* (2016) for a recent review of turbulent Taylor–Couette flow.

Turbulent Taylor rolls have been uncovered in experiments and direct numerical simulations (DNS) by taking temporal averages of the velocity field (Dong 2007; Ravelet *et al.* 2010; Ostilla-Mónico *et al.* 2013; Huisman *et al.* 2014; Ostilla-Mónico *et al.* 2016*a*,*b*), based upon the assumptions that the rolls remain stable and do not travel in the axial direction (z). In most laboratory experiments, the cylinders are bounded by solid end walls, whereas in DNS axially periodic boundary conditions (BC) are usually employed. This renders z homogeneous and enables the usage of short computational domains, which typically accommodate one or two pairs of Taylor rolls (Dong 2007; Brauckmann & Eckhardt 2013; Ostilla-Mónico *et al.* 2016*a*,*b*; Sacco *et al.* 2019). In these computations, typical observation times do not exceed a few hundred convective time units. This raises the question of whether Taylor rolls remain stable and stationary up to arbitrarily long times. In cylindrical RBC cells, for example, the characteristic large-scale circulations (LSC) are known to undergo spontaneous diffusive meandering in the naturally homogeneous (i.e. azimuthal) direction (Sun *et al.* 2005; Brown & Ahlers 2006; Xi *et al.* 2006; Brown & Ahlers 2008). Slow dynamics of the LSC – clearly separated from the time scale of the turbulent fluctuations – was also shown more recently in doubly periodic DNS of rectangular RBC at Rayleigh numbers up to $Ra = 10^7$ (Pandey *et al.* 2018). Similarly, Kreilos *et al.* (2014) found slow spanwise displacements of velocity streaks in turbulent boundary layer and Poiseuille flows.

In this paper, we reveal a transition giving rise to slow, large-scale dynamics in axisymmetric TCF. Beyond a critical domain size, spatio–temporal chaos emerges and the Taylor rolls undergo erratic drifts in z. Compared with the cylinder rotation, the drift speeds are small, but large roll displacements can occur on a slow time scale. We show that the drift statistics are consistent with a Wiener process and characterise the motion with an effective diffusion coefficient of the order of ν.

2. Computer experiments

We perform axisymmetric DNS of corotating Taylor–Couette flow (table 1) with periodic BC in z for moderate Reynolds numbers, allowing for both large computational domains and long integration times at affordable computing costs. We integrate the incompressible Navier–Stokes equations (subject to no-slip BC in r) forward in time (t) using our pseudo-spectral DNS code nsCouette (López *et al.* 2020). The equations are formulated in cylindrical coordinates (r, θ, z) and rendered dimensionless using d, ν/d and d^2/ν (i.e. the characteristic viscous time scale of the problem), as unit length, unit speed and unit time, respectively. In axisymmetric DNS, the θ-dependence is dropped, but all three velocity components are computed.

Ra	Re_i	Re_o	Re_s	R_Ω	Nu_s	Nu	Re_τ	$V(v_R)^{1/2}$	$V(\overline{u}_z)^{1/2}$	D_R
10^5	6726	5865	925	0.14	4.5		32	10^{-14}	10^{-13}	10^{-29}
10^6	21374	18638	2940	0.14	7.4		74	0.4	1.1	0.008
10^7	104223	98156	7138	0.30	10.4	14.4	137	6.4	8.8	0.4
10^7	68892	60072	9475	0.14	12.8	14.7	175	6.3	8.8	0.7
10^7	68892	60072	9475	0.14	12.8		175	2.2	NoFX	0.07
10^7	47971	32547	15779	0.05	14.6	15.3	241	8.0	10.5	2
10^8	214780	187284	29539	0.14	22.4		408	12.0	13.8	3

Table 1. Taylor-roll drift dynamics for $\Gamma = 24$ and $\eta = 0.99$. Listed are control parameters (Ra, Re_i, Re_o, Re_s, R_Ω), response parameters (Nu_s, Nu, Re_τ), standard deviations $V(\alpha)^{1/2}$ of the drift speed, $\alpha = v_R$, the net axial flux, $\alpha = \overline{u}_z$, and the effective diffusion coefficient, D_R, estimated as in figure 2. NoFX stands for no axial flux ($\overline{u}_z = 0$) enforced in the simulation.

Motivated by an exact analogy (Eckhardt *et al.* 2020) between two-dimensional RBC and axisymmetric TCF in the narrow-gap limit ($\eta = r_i/r_o \to 1$), we set $\eta = 0.99$ and vary $Re_s = Ud/\nu$, $R_\Omega = 2d\Omega/U$ and $\Gamma = L_z/d$. Here, $d = r_o - r_i$, is the gap width between the inner (i) and the outer (o) cylinder with radius $r_{i/o}$, L_z is their axial length, $U = u_{\theta,i} - \eta\, u_{\theta,o}$ and $\Omega = u_{\theta,o}/r_o$, where $u_{\theta,i/o}$ denotes the azimuthal speed of the cylinders. An important response parameter is the Nusselt number (Nu_s), which quantifies the transport of angular momentum across the fluid layer (Eckhardt *et al.* 2007; Brauckmann *et al.* 2016; Eckhardt *et al.* 2020). According to the exact Navier–Stokes mapping of Eckhardt *et al.* (2020), flows are mathematically identical as long as $Ra = {Re_s}^2\, R_\Omega(1 - R_\Omega) = \text{const.}$, with $Nu = 1 + (Nu_s - 1)/(1 - R_\Omega)$ and Nu being the usual Nusselt number in RBC.

In a first set of DNS (compiled later in figure 3*a*), we fix all parameters but Γ to investigate the onset of spatio–temporal chaos with respect to the lateral domain size. In a second set (compiled in table 1), we fix Γ and explore the effect of shear (Re_s) and rotation (R_Ω). The initial conditions are chosen to trigger the desired number of Taylor rolls (N_R) necessary to maintain their aspect ratio constant throughout all DNS runs ($N_R/\Gamma = 1$). This is important because the dynamics is known to depend on N_R/Γ (Ostilla-Mónico *et al.* 2015, 2016*a*; Wang *et al.* 2020; Zwirner *et al.* 2020). The highest friction Reynolds number ($Re_\tau = u_\tau d/\nu$, where u_τ is the friction velocity at the cylinder walls) measured in all DNS is 408 (table 1). The spatial resolution in terms of wall units (i.e. based on Re_τ and denoted by $^+$) is at least $0.07 \leqslant \Delta r^+ \leqslant 4.03$ and $\Delta z^+ = 4.89$, which is state of the art in DNS of wall-bounded turbulence (Ostilla-Mónico *et al.* 2016*a*,*b*; Feldmann *et al.* 2021).

3. Drift dynamics

Small domains restrict the dynamics of the system, resulting in nearly stationary rolls. This is apparent from the space–time diagram of the wall-normal velocity (u_r) for $\Gamma = 8$ (figure 1*a*). If we now enlarge the domain ($\Gamma \geqslant 10$, $N_R/\Gamma = 1$), the Taylor rolls undergo large, erratic, collective drifts in z that evolve on a slow time scale (figure 1*b–d*). In a domain with $N_R = 24$ rolls, for example, the most energetic axial mode is always $k_z = 12$ (figure 1*e*), confirming that the space–time representation of u_r is indeed a robust way to identify Taylor rolls and to track their dynamics. Every few viscous time units (e.g. at $t \approx 17.5$), the competition with neighbouring modes (here $k_z \in \{11, 13\}$) represents rare attempts to switch to another state with 11 or 13 pairs of rolls. These attempts, however, remain unsuccessful in all our simulations.

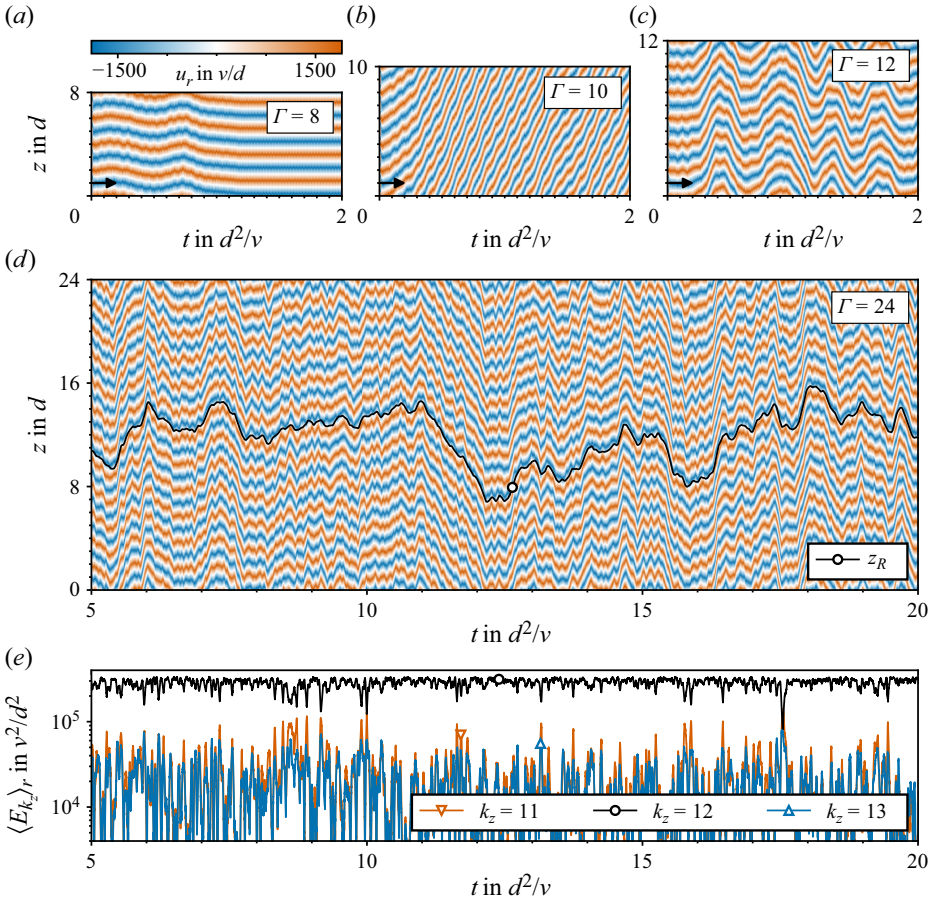

Figure 1. Spatio–temporal dynamics of Taylor rolls for different domain sizes (Γ). Shown are contours of the wall-normal velocity component (u_r) at midgap position extracted from DNS ($Re_s = 9475$ and $R_\Omega = 0.14$ in all cases). Arrows represent 2000 convective time units. (*a*) Stationary Taylor rolls in a small (subcritical) domain. (*b–d*) Axially drifting Taylor rolls in larger (supercritical) domains exhibiting large excursions on a slow time scale. The black line (z_R) plotted on top of the u_r space–time data in (*d*) represents the temporal evolution of the phase angle of the dominant Fourier mode (here $k_z = 12$, corresponding to 12 pairs of rolls). It serves as a proxy for the collective axial displacement of the entire stack of rolls. (*e*) Temporal evolution of the modal kinetic energy, $\langle E_{k_z}\rangle_r$, contained in mode number k_z for the same case as in (*d*); angled brackets denote averaging in the radial direction.

To analyse the drift dynamics quantitatively, we compute axial Fourier spectra of u_r (in particular the u_r midgap space–time data as exemplarily shown in figure 1*d*) and use the phase angle information of the dominant axial mode (here $k_z = 12$) to approximate the collective displacement of the Taylor rolls (z_R), as done earlier by Sacco *et al.* (2019). The temporal evolution of z_R (figure 1*d*) aligns well with u_r, thereby confirming the suitability of z_R to quantify the collective axial drift of the Taylor rolls. For $\Gamma \leqslant 8$, the rolls first undergo slow transient drifts in the beginning of the simulation and then ultimately oscillate with tiny amplitudes and high frequencies about a statistically steady state (figure 2*a*). This fast dynamics of the rolls was reported earlier for three-dimensional turbulent TCF in a domain accommodating one pair of rolls (Sacco *et al.* 2019). By contrast, for $\Gamma = 10$, the rolls wander more than $100d$ before turning back for the first

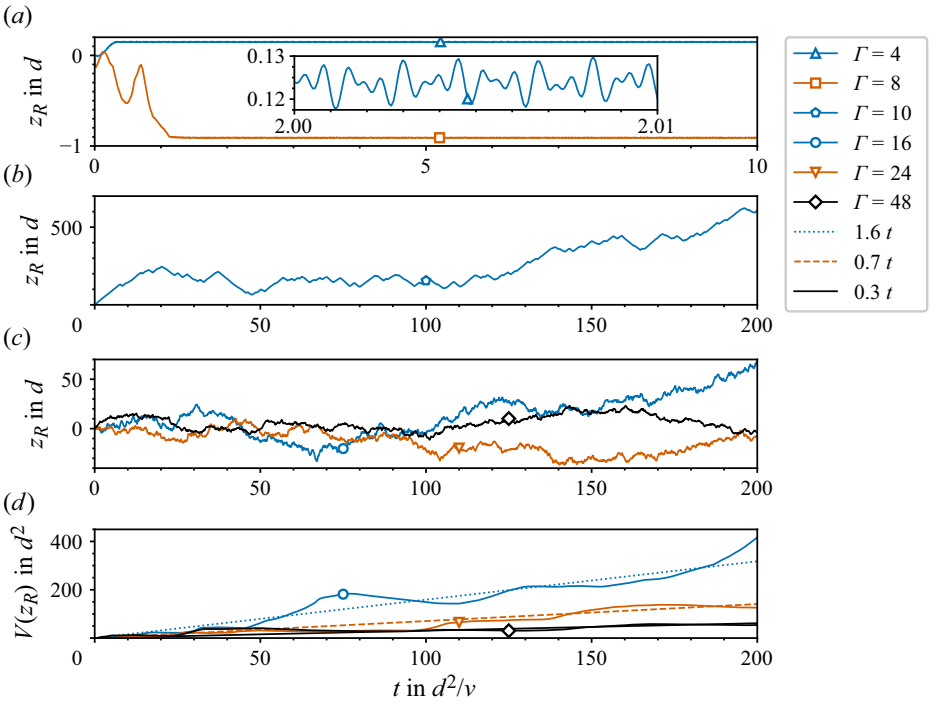

Figure 2. Time series of the axial displacement of Taylor rolls (z_R) for different Γ at $Re_s = 9475$, $R_\Omega = 0.14$. (*a*) Chaotic small-scale oscillations about a fixed axial location in short (subcritical) domains ($\Gamma \in [4, 8]$). The simulations span more than 200 viscous time units (d^2/ν), without reflecting any change of this behaviour; except for the initial transients in the first two viscous time units of the simulations, which we discard for all further analyses in all cases. (*b*) Huge erratic axial drifts in a larger (supercritical) domain close to the critical point ($\Gamma = 10$). (*c*) Large erratic axial drifts with qualitatively similar dynamics in larger (supercritical) domains ($\Gamma \in [16, 24, 48]$). (*d*) Temporal evolution of the displacement variance, $V(z_R)$, for the data sets shown in (*c*). The slope of the corresponding linear fit (broken lines) serves as an estimate for the effective diffusion coefficient for the drift dynamics.

time, and continue moving erratically thereafter (figure 2*b*). With further increasing Γ, these excursions persist but become less extreme (figure 2*c*).

We quantify the Taylor-roll motion statistically by computing the variance of the axial displacement, $V(z_R, t) = \langle z_R^2 \rangle_t - \langle z_R \rangle_t^2$, where angled brackets denote temporal averaging up to time t. For $\Gamma \leqslant 8$, the fast dynamics of the rolls is centred around a fixed location and $V(z_R)$ quickly saturates to a constant, in agreement with Sacco *et al.* (2019), who reported Gaussian fluctuations of z_R with constant variance. By contrast, for $\Gamma \geqslant 10$, $V(z_R)$ grows approximately linearly with time, as in a Wiener process (figure 2*d*). The drift of the rolls can thus be characterised with an effective diffusion coefficient, D_R, as the slope of a linear fit to the variance. For all our analyses, we use time series of at least 200 viscous time units and we generally discard the first $2d^2/\nu$ to exclude initial transients.

4. Transition to large erratic drift dynamics

The dependence of the diffusion coefficient D_R on the domain size Γ is shown in figure 3 for a fixed Rayleigh number ($Ra = 10^7$). Our data suggest a divergence of D_R near a critical point ($\Gamma_c = 9.99$) followed by a monotonic decrease as Γ increases. To examine the nature of this transition, we compare spatial and temporal Fourier spectra from sub-

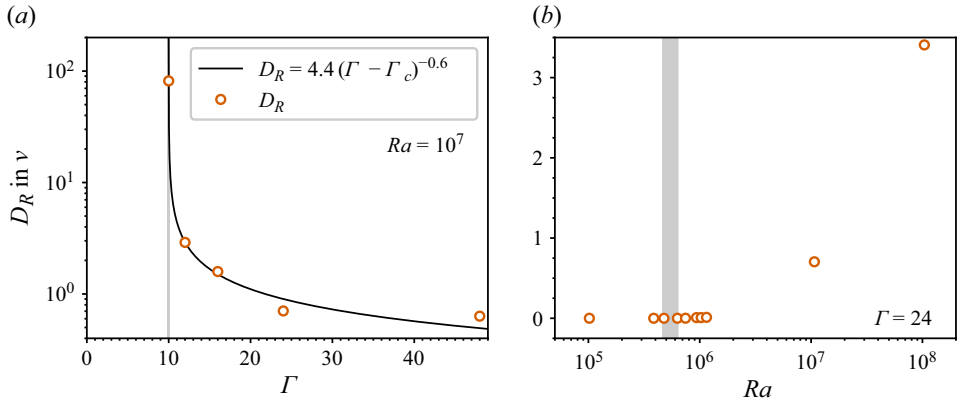

Figure 3. Transition to large, erratic drift dynamics of Taylor rolls. (*a*) Beyond a critical domain size (grey line, $\Gamma_c = 9.99$ from a power-law fit to the data), the Taylor-roll drift can be characterised by an effective diffusion coefficient, D_R, as shown in figure 2(*d*); here for $Ra = 10^7$, $Re_s = 9475$ and $R_\Omega = 0.14$. Note, that Γ must take even integer values in order to maintain a unit aspect ratio of the Taylor rolls. (*b*) For a fixed domain size ($\Gamma = 24$), the Taylor-roll drift starts at a critical Rayleigh number, $Ra_c \approx 6 \times 10^5$, and becomes more pronounced as Ra increases. The grey region denotes the uncertainty in determining Ra_c; it spans the interval between the last run with $D_R = 0$ and the first run with $D_R > 0$.

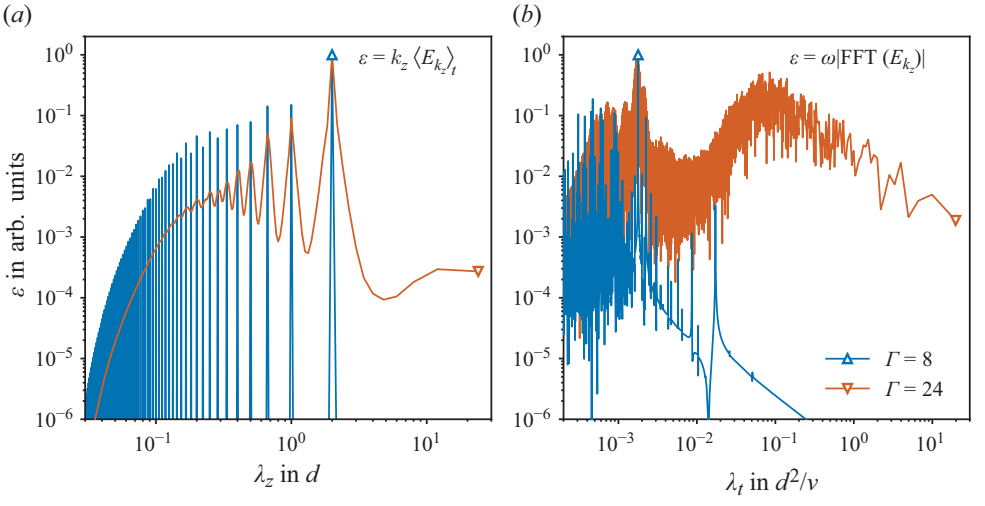

Figure 4. Transition from temporal to spatio–temporal chaos for increasing Γ. Shown are premultiplied energy spectra, $\varepsilon(\lambda)$, at $Re_s = 9475$ and $R_\Omega = 0.14$ from a subcritical ($\Gamma = 8$) and a supercritical ($\Gamma = 24$) domain. Spectra for other Γ look very similar and are thus not shown here. (*a*) Premultiplied spectra of the modal kinetic energy (as, for example, in figure 1*e*) versus axial wavelengths, $\lambda_z = 2\pi/\kappa_z$, where κ_z is the axial wavenumber and angled brackets denote temporal averaging. (*b*) Premultiplied temporal Fourier spectra of the modal kinetic energy (as, for example, in figure 1*e*) for the dominant mode (here, for example, for $k_z = 4$ in the case of $\Gamma = 8$) versus temporal wavelengths, $\lambda_t = 2\pi/\omega$, where ω is the angular frequency. FFT means fast Fourier transform.

and supercritical domains (figure 4). For $\Gamma = 8$, the axial spectrum of u_r presents discrete peaks at wavelength $\lambda_z = 2d$ and its harmonics only (figure 4*a*). This implies that the flow state consists of four perfectly synchronised copies of one pair of Taylor rolls. In fact, when comparing this state to those obtained for $\Gamma \in \{2, 4\}$, the same Nusselt numbers, $\langle Nu_s \rangle = 12.82474 \pm 0.00002$, and spectra (not shown here) are recovered. By contrast, the

states obtained for $\Gamma \geqslant 10$ exhibit continuous spatial spectra (e.g. for $\Gamma = 24$ in figure 4*a*), indicating spatial defects in the roll structure, i.e. there are no identical rolls in the entire stack. A similar transition to spatio–temporal chaos was reported before for axially oscillated (Avila *et al.* 2007) and hydromagnetic (Guseva *et al.* 2015) Taylor–Couette flow. For both, however, no slow large-scale drift of the roll patterns was reported, possibly due to much shorter simulation times.

The transition to spatio–temporal chaos also alters the temporal spectra (figure 4*b*). For $\Gamma < \Gamma_c$, the temporal spectrum is continuous, indicating temporal chaos, and exhibits a peak at $2 \times 10^{-3} d^2/\nu$ (i.e. approximately 20 convective time units) before falling sharply. This peak is associated with the fast, small-displacement dynamics with $D_R = 0$ and Gaussian statistics reported by Sacco *et al.* (2019). For $\Gamma > \Gamma_c$, the temporal spectrum features an additional broad peak at approximately $0.1 d^2/\nu$, corresponding to the slow drift dynamics characterised by a Wiener process (i.e. $D_R > 0$ and linearly increasing variance). The transition to spatio–temporal chaos is also reflected in the mean Nusselt number, but only in the third digit; $\langle Nu_s \rangle = 12.76 \pm 0.04$ for all $\Gamma \geqslant 10$. We note that while much effort has been dedicated to remove drifts in the analysis of turbulent dynamics of wall-bounded flows (Willis *et al.* 2013; Budanur *et al.* 2015), here the onset of spatio–temporal chaos appears intrinsically linked to the slow, erratic drift dynamics.

5. Dependence of the drift dynamics on the flow configuration

We exploit the analogy between TCF and RBC (Bradshaw 1969; Veronis 1970; Prigent *et al.* 2006; Eckhardt *et al.* 2007, 2020) to demonstrate that the drift dynamics is found throughout the centrifugally unstable corotating regime. According to the exact Navier–Stokes mapping of Eckhardt *et al.* (2020), axisymmetric TCF systems in the narrow-gap limit ($\eta \to 1$) are exactly identical if $Ra = {Re_s}^2\, R_\Omega (1 - R_\Omega) = \text{const.}$, i.e. the large-scale drift dynamics is identical as well. Indeed, for moderate outer cylinder rotation ($R_\Omega \in \{0.14, 0.30\}$), the drift statistics are similar (table 1, compare rows 3 and 4) and the same is true for the corrected Nusselt number, $Nu = 1 + (Nu_s - 1)/(1 - R_\Omega)$. We attribute the small deviations to small, yet finite, curvature effects ($\eta = 0.99 < 1$), which are not included in the analogy. For very slow outer cylinder rotation ($R_\Omega = 0.05$), the drift statistics deviate noticeably (table 1, compare rows 3, 4 and 6). This is as expected because the exact analogy breaks down in the limit of a stationary outer cylinder ($R_\Omega = 0$).

Next, we fix $R_\Omega = 0.14$ and $\Gamma = 24$, and vary Re_s, thereby varying the Rayleigh number (figure 3*b*). At low Ra, the rolls are stationary, as observed for low Γ in § 3. Similarly, at a critical point ($Ra_c \approx 6 \times 10^5$), the rolls begin to drift in the axial direction. As Ra is increased beyond this critical point, the diffusion coefficient of the drift increases. This is contrary to the effect of increasing Γ, but consistent with RBC experiments (Xi *et al.* 2006), where the rate of erratic rotations of the LSC increases tenfold as Ra increases from 10^9 to 10^{10}. A two-dimensional parametric study of the combined effect of Γ and Ra would be interesting, but expensive and thus out of the scope of this work.

The axial drift of the Taylor rolls is associated with a net mass flux in z with mean speed $\overline{u}_z$. This flux is strongly correlated to the drift speed ($v_R = \dot{z}_R = \partial z_R/\partial t$) of the rolls (figure 5*a*), and raises the question of whether the roll displacement causes the net axial flux or *vice versa*. The fact that v_R is approximately $500 d/U$ ahead of $\overline{u}_z$ suggests the former (figure 5*b*). We probe this hypothesis by enforcing $\overline{u}_z = 0$, as in laboratory experiments of TCF with end walls. In our DNS with axially periodic BC, we enforce $\overline{u}_z = 0$ by imposing an appropriate adverse pressure gradient at each time step. This technique was previously applied to successfully compare axially periodic simulations to lab experiments for Taylor–Couette flow in the counter-rotating regime (Edwards *et al.*

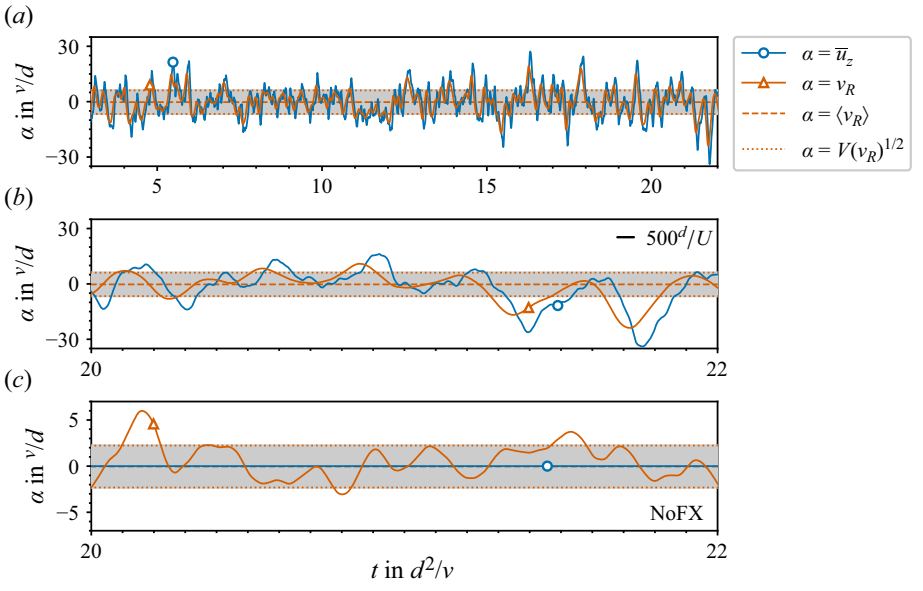

Figure 5. Taylor-roll dynamics with and without axial flux constraint for otherwise identical parameters ($Re_s = 9475$, $R_\Omega = 0.14$, $\Gamma = 24$). (*a*) Time series of the drift speed of the Taylor rolls ($v_R = \dot{z}_R = \partial z_R/\partial t$) and the net axial flux ($\overline{u}_z$) for the case in figure 1(*d*). (*b*) Close-up to the data in (a). As a visual reference, the black dash represents 500 convective time units. (*c*) Time series from a simulation with no axial flux (NoFX, i. e. $\overline{u}_z = 0$) enforced.

1991), with radial heating (Ali & Weidman 1990) and with axially oscillating inner cylinder (Marques & Lopez 1997; Avila *et al.* 2007).

As a result of suppressing the axial mass flux, v_R, $V(v_R)$ and D_R are substantially reduced (figure 5*c*, table 1, compare rows 4 and 5), but when rescaled, the drift dynamics remains qualitatively unaltered (figure 6*a*). Specifically, $V(z_R)$ still increases linearly with time (figure 6*e*), although at a slower pace.

6. Discussion

We have shown that axisymmetric Taylor–Couette flows exhibit a transition to spatio–temporally chaotic Taylor rolls that drift erratically in the axial direction. At long time scales, the drift motion is diffusive and can lead to very large displacements. Future works should clarify whether this dynamics persists in three-dimensional TCF simulations and in experiments with end walls. We note that even with walls, flow patterns can drift in z with phase being created/annihilated near the walls (Heise *et al.* 2008).

In figure 6 the roll displacements extracted from our DNS are compared to the azimuthal meandering of the large-scale circulation in circular Rayleigh–Bénard convection (Brown & Ahlers 2006; Xi *et al.* 2006) and spanwise streak displacements in Poiseuille flow (Kreilos *et al.* 2014). For the sake of comparison, we converted the rotation angle of the LSC to a length scale as $z_R(t) = R\,\theta(t)$ using the radius (R) of the RBC cell. Additionally, we rescaled all drift signals to the viscous time unit, which is also the relevant one of the exact analogy (Eckhardt *et al.* 2020). The qualitative agreement is remarkable and suggests that this slow dynamics might be inherent to large-scale motions in many fluid systems. However, longer RBC and Poiseuille flow runs would be needed to confirm the Wiener statistics found here for Taylor–Couette flow, and to estimate the corresponding diffusion coefficients (figure 6*b–e*). Additional statistical analyses and

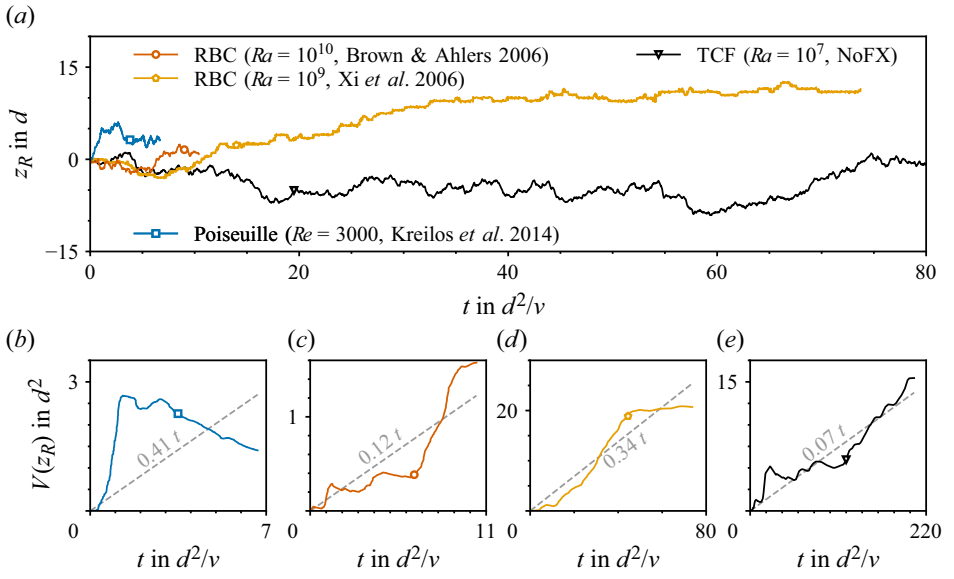

Figure 6. Comparison of large-scale drifts (z_R) among different set-ups and fluid systems. (*a*) Taylor-roll drift in Taylor–Couette flow with no axial flux (NoFX, $\bar{u}_z = 0$); same run as in figure 5(*c*). Azimuthal meandering of a single convection roll in cylindrical Rayleigh–Bénard convection for laboratory experiments lasting 11 days ($Ra = 10^{10}$, Brown & Ahlers (2006)) and 33 days ($Ra = 10^9$, Xi *et al.* (2006)), respectively. Spanwise streak displacement in Poiseuille flow DNS (Kreilos *et al.* 2014). (*b–e*): Corresponding displacement variance, $V(z_R)$, including linear fits (broken lines) to demonstrate an approximate linear growth with time and to estimate an effective diffusion coefficient (D_R).

modelling strategies previously applied to three-dimensional RBC (Brown & Ahlers 2007, 2008) could help elucidate further aspects of the drift dynamics reported here and deepen this comparison. A particularly intriguing question is whether the rare cessation events reported for Rayleigh–Bénard convection have a counterpart in Taylor–Couette flow. This would correspond to a sudden decay and resurgence of Taylor rolls at a different location (possibly with a change of the number of rolls). While such events were not observed here, our data suggests that they may occur; see, for example, the event at $t \approx 17.5$ in figure 1*(e)*.

We stress that the shortest time series considered here (figure 2) correspond to $200Re_s = \mathcal{O}(10^6)$ convective time units and to $200\sqrt{Ra} = \mathcal{O}(10^5)$ free-fall time units in RBC ($Ra = 10^7$). These observation times are comparable to those used to characterise large-scale states in RBC (Pandey *et al.* 2018; Wang *et al.* 2020), but they are several orders of magnitudes longer compared with typical observation times in high-Re TCF studies (Brauckmann & Eckhardt 2013; Huisman *et al.* 2014; Ostilla-Mónico *et al.* 2016*a*,*b*; Sacco *et al.* 2019). In the Taylor–Couette apparatus of Huisman *et al.* (2014), for example, this would correspond to a measurement time of two weeks.

Acknowledgements. We appreciate stimulating discussions with A. Vela-Martín and D. Morón.

Funding. We gratefully acknowledge the received financial support from the German Research Foundation (DFG) through the priority programme Turbulent Superstructures (SPP1881) and computational resources provided by the North German Supercomputing Alliance (HLRN) through project hbi00041.

Declaration of interests. The authors report no conflict of interest.

Data availability statement. The data that support the findings of this study will be made openly available in Pangaea at https://doi.pangaea.de/10.1594/PANGAEA.974809.

References

Ali, M. & Weidman, P.D. 1990 On the stability of circular couette flow with radial heating. *J. Fluid Mech.* **220**, 53–84.

Avila, M., Marques, F., Lopez, J.M. & Meseguer, A. 2007 Stability control and catastrophic transition in a forced Taylor–Couette system. *J. Fluid Mech.* **590**, 471–496.

Bradshaw, P. 1969 The analogy between streamline curvature and buoyancy in turbulent shear flow. *J. Fluid Mech.* **36** (1), 177–191.

Brauckmann, H.J. & Eckhardt, B. 2013 Direct numerical simulations of local and global torque in Taylor-Couette flow up to Re = 30 000. *J. Fluid Mech.* **718**, 398–427.

Brauckmann, H.J., Salewski, M. & Eckhardt, B. 2016 Momentum transport in Taylor–Couette flow with vanishing curvature. *J. Fluid Mech.* **790**, 419–452.

Brown, E. & Ahlers, G. 2006 Rotations and cessations of the large-scale circulation in turbulent rayleigh–Bénard convection. *J. Fluid Mech.* **568**, 351.

Brown, E. & Ahlers, G. 2007 Large-Scale circulation model for turbulent Rayleigh–Bénard convection. *Phys. Rev. Lett.* **98** (13), 134501.

Brown, E. & Ahlers, G. 2008 A model of diffusion in a potential well for the dynamics of the large-scale circulation in turbulent Rayleigh–Bénard convection. *Phys. Fluids* **20** (7), 075101.

Budanur, N.B., Cvitanović, P., Davidchack, R.L. & Siminos, E. 2015 Reduction of SO(2) symmetry for spatially extended dynamical systems. *Phys. Rev. Lett.* **114** (8), 1–5.

Coles, D. 1965 Transition in circular Couette flow. *J. Fluid Mech.* **21** (3), 385–425.

Dauxois, T. *et al.*et al. 2021 Confronting grand challenges in environmental fluid mechanics. *Phys. Rev. Fluids* **6** (2), 020501.

Dong, S. 2007 Direct numerical simulation of turbulent Taylor–Couette flow. *J. Fluid Mech.* **587**, 373–393.

Eckhardt, B., Doering, C.R. & Whitehead, J.P. 2020 Exact relations between Rayleigh–Bénard and rotating plane Couette flow in two dimensions. *J. Fluid Mech.* **903** (Busse 2012), R4.

Eckhardt, B., Grossmann, S. & Lohse, D. 2007 Fluxes and energy dissipation in thermal convection and shear flows. *Europhys. Lett. (EPL)* **78** (2), 24001.

Edwards, W.S., Tagg, R.P., Dornblaser, B.C., Swinney, H.L. & Tuckerman, L.S. 1991 Periodic traveling waves with nonperiodic pressure. *Eur. J. Mech. (B/Fluids)* **10** (2), 205–210.

Feldmann, D., Borrero-Echeverry, D., Burin, M.J., Avila, K. & Avila, M. 2023 Routes to turbulence in taylor–Couette flow. *Phil. Trans. R. Soc. A: Math. Phys. Engng Sci.* **381** (2246),

Feldmann, D., Morón, D. & Avila, M. 2021 Spatiotemporal intermittency in pulsatile pipe flow. *Entropy* **23** (1), 1–19.

Fenstermacher, P.R., Swinney, H.L. & Gollub, J.P. 1979 Dynamical instabilities and the transition to chaotic Taylor vortex flow. *J. Fluid Mech.* **94** (1), 103–128.

Grossmann, S., Lohse, D. & Sun, C. 2016 High-Reynolds number Taylor–Couette turbulence. *Annu. Rev. Fluid Mech.* **48** (1), 53–80.

Guseva, A., Willis, A.P., Hollerbach, R. & Avila, M. 2015 Transition to magnetorotational turbulence in taylor-couette flow with imposed azimuthal magnetic field. *New J. Phys.* **17** (9), 093018.

Heise, M., Hoffmann, Ch, Abshagen, J., Pinter, A., Pfister, G. & Lücke, M. 2008 Stabilization of domain walls between traveling waves by nonlinear mode coupling in Taylor–Couette flow. *Phys. Rev. Lett.* **100** (6), 064501.

Huisman, S.G., Van Der, V., Roeland, C.A., Sun, C. & Lohse, D. 2014 Multiple states in highly turbulent Taylor–Couette flow. *Nat. Commun.* **5** (1), 1–5.

Kreilos, T., Zammert, S. & Eckhardt, B. 2014 Comoving frames and symmetry-related motions in parallel shear flows. *J. Fluid Mech.* **751**, 685–697.

Lathrop, D.P., Fineberg, J. & Swinney, H.L. 1992 Transition to shear-driven turbulence in Couette–Taylor flow. *Phys. Rev. A* **46** (10), 6390–6405.

López, J.M., Feldmann, D., Rampp, M., Vela-Martín, A., Shi, L. & Avila, M. 2020 nsCouette - a high-performance code for direct numerical simulations of turbulent Taylor–Couette flow. *SoftwareX* **11**, 100395.

Marques, F. & Lopez, J.M. 1997 Taylor–Couette flow with axial oscillations of the inner cylinder: Floquet analysis of the basic flow. *J. Fluid Mech.* **348**, 153–175.

Ostilla-Mónico, R., Lohse, D. & Verzicco, R. 2016*a* Effect of roll number on the statistics of turbulent Taylor–Couette flow. *Phys. Rev. Fluids* **1** (5), 054402.

Ostilla-Mónico, R., Stevens, R.J.A.M., Grossmann, S., Verzicco, R. & Lohse, D. 2013 Optimal Taylor–Couette flow: direct numerical simulations. *J. Fluid Mech.* **719**, 14–46.

Ostilla-Mónico, R., Verzicco, R., Grossmann, S. & Lohse, D. 2016*b* The near-wall region of highly turbulent Taylor–Couette flow. *J. Fluid Mech.* **788**, 95–117.

OSTILLA-MÓNICO, R., VERZICCO, R. & LOHSE, D. 2015 Effects of the computational domain size on direct numerical simulations of Taylor–Couette turbulence with stationary outer cylinder. *Phys. Fluids* **27** (2), 025110.

PANDEY, A., SCHEEL, J.D. & SCHUMACHER, J. 2018 Turbulent superstructures in Rayleigh–Bénard convection. *Nat. Commun.* **9** (1), 1–11.

PRIGENT, A., DUBRULLE, B., DAUCHOT, O. & MUTABAZI, I. 2006 The Taylor–Couette flow: the hydrodynamic twin of Rayleigh–Bénard convection. In *Dynamics of Spatio-Temporal Cellular Structures*, (ed. MUTABAZI I., WESFREID J.E. & GUYON E.),Springer Tracts in Modern Physics, vol. 207, pp. 225–242. Springer New York.

RAVELET, F., DELFOS, R. & WESTERWEEL, J. 2010 Influence of global rotation and Reynolds number on the large-scale features of a turbulent Taylor–Couette flow. *Phys. Fluids* **22** (5), 1–8.

SACCO, F., VERZICCO, R. & OSTILLA-MÓNICO, R. 2019 Dynamics and evolution of turbulent Taylor rolls. *J. Fluid Mech.* **870**, 970–987.

SMITS, A.J., MCKEON, B.J. & MARUSIC, I. 2011 High-Reynolds number wall turbulence. *Annu. Rev. Fluid Mech.* **43** (1), 353–375.

SUN, C., XI, H.-D. & XIA, K.-Q. 2005 Azimuthal symmetry, flow dynamics, and heat transport in turbulent thermal convection in a cylinder with an aspect ratio of 0.5. *Phys. Rev. Lett.* **95** (7), 074502.

TAYLOR, G.I. 1923 Stability of a viscous liquid contained between two rotating cylinders. *Phil. Trans. R. Soc. Lond. Ser. A, Contain. Pap. Math. Phys. Charact.* **223** (605-615), 289–343.

VERONIS, G. 1970 The analogy between rotating and stratified fluids. *Annu. Rev. Fluid Mech.* **2** (1), 37–66.

WANG, Q., VERZICCO, R., LOHSE, D. & SHISHKINA, O. 2020 Multiple states in turbulent large-aspect-ratio thermal convection: what determines the number of convection rolls? *Phys. Rev. Lett.* **125** (7), 074501.

WILLIS, A.P., CVITANOVIĆ, P. & AVILA, M. 2013 Revealing the state space of turbulent pipe flow by symmetry reduction. *J. Fluid Mech.* **721**, 514–540.

XI, H.-D., ZHOU, Q. & XIA, K.-Q. 2006 Azimuthal motion of the mean wind in turbulent thermal convection. *Phys. Rev. E* **73** (5), 056312.

ZWIRNER, L., TILGNER, A. & SHISHKINA, O. 2020 Elliptical instability and multiple-roll flow modes of the large-scale circulation in confined turbulent Rayleigh–Bénard convection. *Phys. Rev. Lett.* **125** (5), 054502.